Lenhart, A., Jackson, C.A.-L., Bell, R.E., Duffy, O.B., Gawthorpe, R.L., and Fossen, H., 2019, Structural architecture and composition of crystalline basement offshore west Norway: Lithosphere, https://doi.org/10.1130/L668.1.

GSA Data Repository Item 2019086

Item DR1:

Noise filtering of seismic reflection data

Data acquisition and processing reports of 2D and 3D reflection seismic surveys used in this study are not accessible. Hence, it is unknown whether e.g. the amplitudes of seismic reflections are 'real', or if they have been enhanced during processing. However, the relative difference in amplitude strength should be preserved in the data. The post-processing frequency content of 3D seismic volumes was analysed using GeoTeric seismic interpretation software (e.g. Figure 1.1A and Table 1; www.geoteric.com), and the average intra-crystalline basement frequency within the 3D seismic data ranges from 10 to 30 Hz. To improve the signal to noise ratio and imaging of intra-basement reflections, 3D seismic volumes were filtered to reduce coherent and random noise using standard filtering workflows in GeoTeric (e.g. Figure 1.1).

The coherent noise filter is a structurally oriented, edge-preserving filter which removes minor acquisition and migration noise while preserving small details like edges and sharp dips within a structure. Prior to coherent noise filtering, dip and azimuth steering volumes were created to optimally orientate the filter along reflectors. Different filter sizes were tested, with a 9x9x11 filter size for the dip and azimuth steering volumes and a filter length of 5 for the coherent noise filter producing the best results. Larger filter sizes resulted in pronounced smoothing of reflectors and loss of geological information, whereas smaller filters did not remove noise effectively. The numbers in the filter size represent voxel ('volume pixel'), and a filter length of 5 signifies that the operator considers 2 samples on

either side of the voxel in question. The signal to noise ratio within crystalline basement is improved after coherent noise filtering, and intra-basement reflections appear more continuous and jitter is significantly reduced (Figure 1.1C).

After removing coherent noise from the seismic data, an additional random noise filter was applied. This filter is a structurally oriented low-pass filter that improves reflector continuity whilst preserving subtle discontinuities. The main differences to the coherent noise filter are that: i) no pre-computed dip and azimuth steering volumes are required; ii) the filter works particularly well in chaotic seismic facies; iii) it improves the continuity of very thin events, and iv) it is very sensitive to small-scale discontinuities. The filtering process was run with five iterations and a very small smoothing factor (i.e. 0.1) to preserve the actual reflector geometry. Although the differences are fairly small, the removal of random noise resulted in an even clearer image of intra-basement reflections than the coherent noise filter alone (Figure 1.1D).

To ensure that no geological information has been removed from the datasets, difference volumes of 3D seismic data before and after noise filtering have been computed (Figure 1.1E and F). Results indicate that within crystalline basement, no coherent (structured) signals have been removed, but some higher-amplitude, semi-coherent signals at Top Basement level have been eliminated during the filtering process. However, due to the relative difference in amplitude between the Top Basement reflection and the noise, high-amplitude areas such as the Top Basement reflections will often result in a high-amplitude difference, even if minimal noise attenuation has been applied.

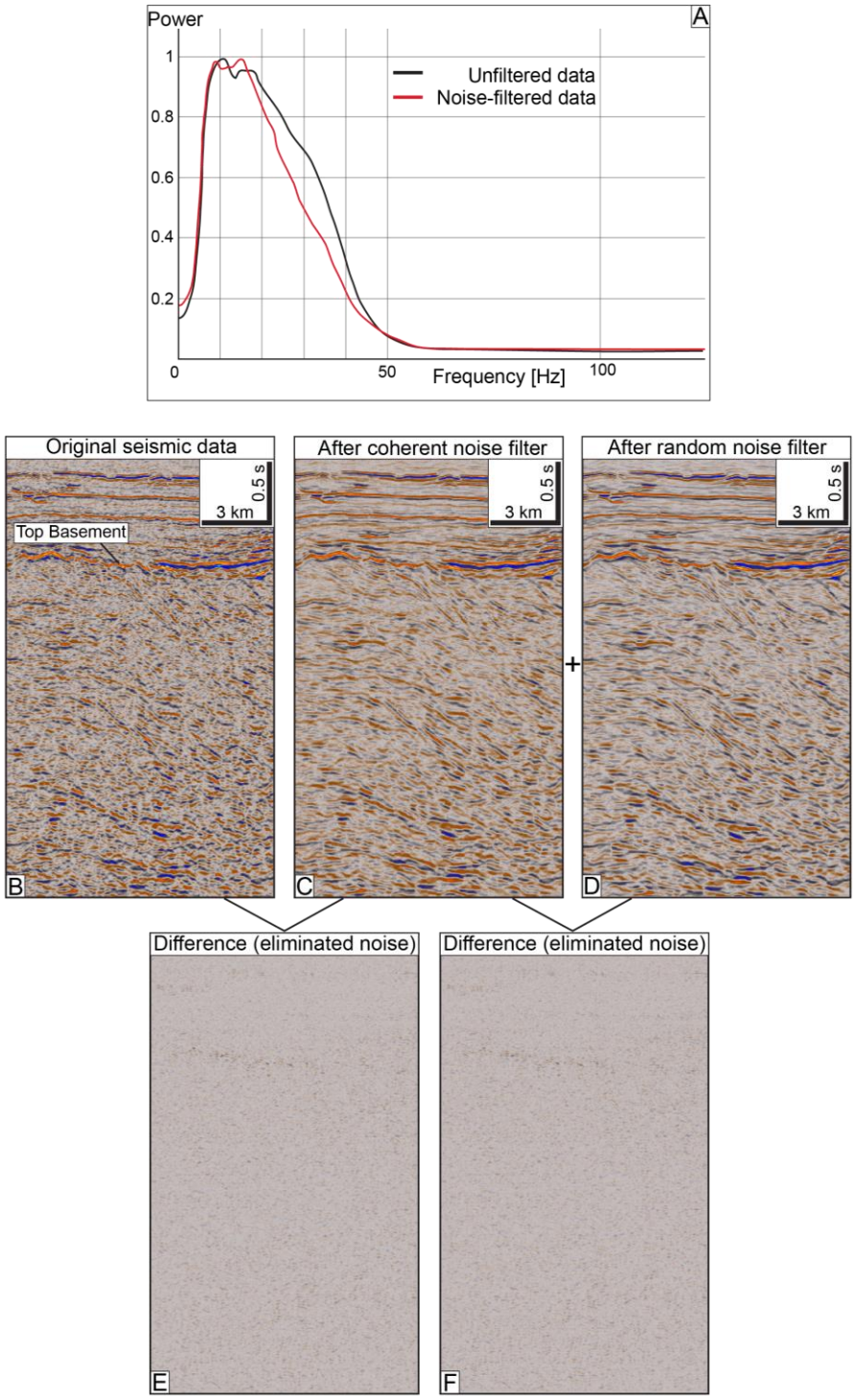

Figure DR1.1: Effect of coherent and random noise filters on imaging clarity and total frequency content within crystalline basement for seismic volume ST98M8. A) Frequency spectrum within crystalline basement before and after noise filtering. Noise filtering results in a slight reduction of the bandwidth between 30-40 Hz and hence, decreased seismic resolution. See Table DR1.1 for details. B) Original, unfiltered seismic data showing a representative section through intra-basement reflectivity. Reflections are more continuous and contain less jitter. C) Same seismic section as shown in B after applying coherent noise filter. D) After applying random noise filter on top of coherent noise filter. E and F) Difference between filtered and unfiltered seismic data to illustrate what has been removed from the data.

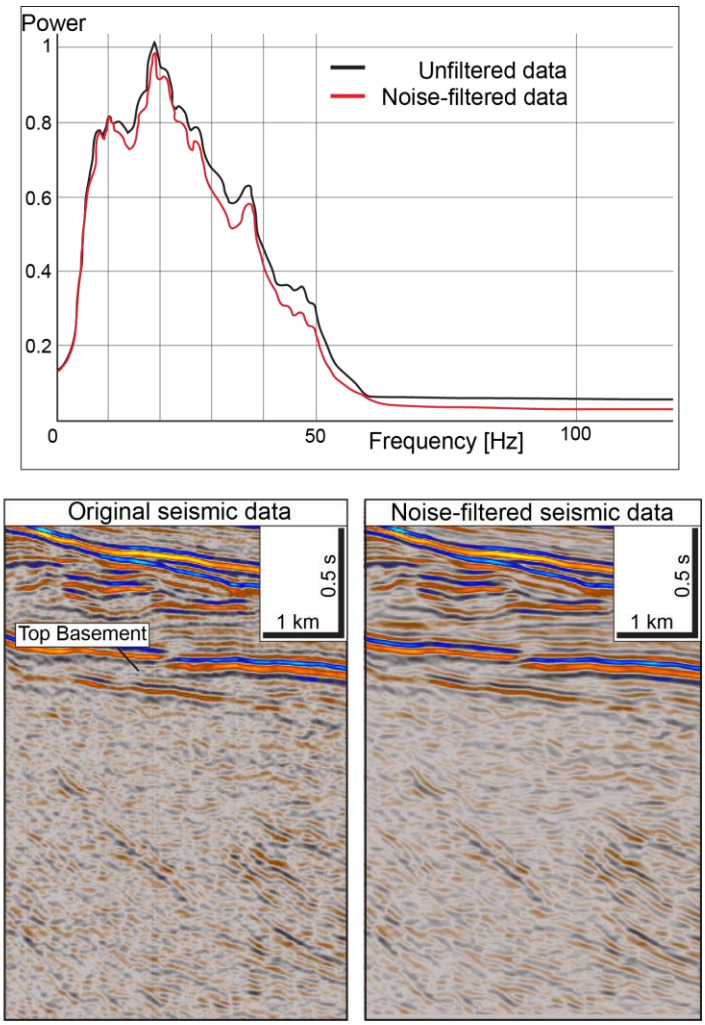

Figure DR1.2: Effect of coherent and random noise filters on imaging clarity and total frequency content within crystalline basement for seismic volume NH9805M99.

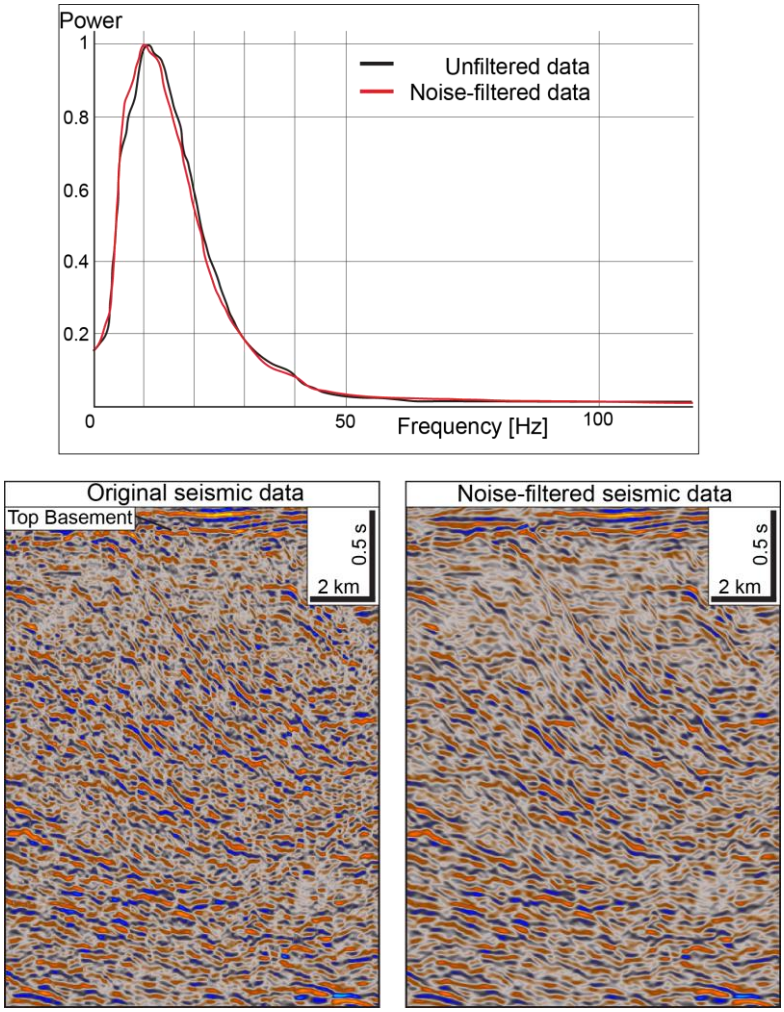

Figure DR1.3: Effect of coherent and random noise filters on imaging clarity and total frequency content within crystalline basement for seismic volume MS97M.

To assess and quantify how noise filtering affected the frequency content of 3D seismic data sets, frequency spectra, as well as the mean and dominant frequency, bandwidth have been computed for un-filtered and noise-filtered data (Figure DR1.1A, DR1.2, DR1.3, and Table DR1.1). Table DR1.1 indicates that for all three noise-filtered seismic volumes a small reduction in bandwidth is observed. The dominant frequency within crystalline basement did not change significantly after noise filtering, apart from seismic volume ST98M8 (Figure DR1.1A), where an increase of nearly 4 Hz is observed. Based on these observations, we conclude that noise filtering did not noticeably change the frequency content of 3D seismic volumes, and hence, did not further decrease seismic resolution within crystalline basement. Comparing the amplitude content of 3D seismic data sets before and after noise filtering, we observe that the amplitudes of intra-basement reflections did not change. Therefore, we

conclude that the noise filtering process has no effect on the characteristics and amplitude content of intra-basement seismic facies.

Table DR1.1: Frequency content within crystalline basement for 3D seismic volumes before and after noise filtering.

	Frequency Information					
	Unfiltered Data			Noise-filtered Data		
Seismic Volume	Dominant Frequency	*Bandwidth	Mean Frequency	Dominant Frequency	*Bandwidth	Mean Frequency
ST98M8	11.7 Hz	30.2 Hz	25.25 Hz	15.6 Hz	24.4 Hz	27.75 Hz
NH9805M99	19.5 Hz	33.2 Hz	32.65 Hz	19.5 Hz	32.2 Hz	29.26 Hz
MS97M	11.7 Hz	15.6 Hz	18.64 Hz	10.7 Hz	14.6 Hz	19.76 Hz

*Bandwidth is measured at 0.5 Power

Item DR2:

3D velocity model and depth conversion of seismic data

3D seismic reflection data were depth converted using the velocity model building process which is implemented in Petrel E&P software by Schlumberger. The velocity model was divided into 6 layers which are defined by the interpreted horizons of the seafloor, Base Pleistocene unconformity, Base Tertiary unconformity, Top Blodøks (Upper Cretaceous), Top Basement and Top Western Gneiss Region (WGR). Where available, time-depth-relationships (TDR's) from wells where used for depth conversion of the entire sediment column down to the crystalline basement. Within the basement, a velocity sensitivity study was conducted using a range of plausible P-wave velocity values for allochthonous material and Gneiss (WGR). Estimated P-wave velocities for the uppermost part of the basement are based on checkshot data (where available) and published literature (e.g. Birch, 1960; Christensen, 1965; Ullemeyer et al., 2006). The velocity (V) within each model layer was calculated using the linear relationship V=V0+K*(Z-Z0), where V0 is the velocity at the top

of the layer, K is the gradient which defines the linear velocity increase with depth, and Z-Z0 represents the distance between the top of the layer and each XY location (in length units). Velocity-depth relationships for metamorphic rocks under different lithostatic pressure conditions were used to estimate K (Wang et al., 2005).

Overall, nine different velocity models were created and their effect on the dip angle of the reflection of an intra-basement fault plane was tested (Table DR2.1). The velocity model chosen for the depth conversion of the 3D seismic data (Model 9) uses a velocity of 4900 m/s at Top Basement level and 6320 m/s for the WGR. K-values for the Allochthons and the WGR are -0.17 and -0.025, respectively. This model was chosen because its P-wave velocities are closest to the available velocity information from borehole data and because the dip angle (39°) of an intra-basement fault plane reflection is still plausible for normal faults. The error in the dip angle of intra-basement reflections is based on the velocity model sensitivity study and amounts to c. ±7°.

We would like to point out that depth conversion of post-stack time-migrated data is generally difficult and associated with considerable errors and uncertainties. We assume that the acquisition of the seismic data was not designed to properly illuminate basement structures in the first place and that the processing of the data and velocity model that was used for migration are not accurate, which complicates depth conversion. Furthermore, the utilized velocity model building process is a simplification and it is based on the assumption of a layer-cake geometry of the subsurface. Hence, big uncertainties are associated with areas where pronounced lateral changes in velocities are observed, e.g. where sediments are in contact with rotated basement fault blocks. However, we think our model is still sufficient for the purpose of this study which focuses on the overall geometry of large-scale, deep intra-basement structures.

Table DR2.1: Velocity models

	Model 1	Model 2	Model 3	Model 4	Model 5	Model 6	Model 7	Model 8	Model 9
P-wave velocity Allochthon [m/s]	Well TDR	3680	4500	4500	4500	4700	4900	5000	4900
K value (Allochthon)	Well TDR	-0.46	-0.25	-0.2	-0.33	-0.25	-0.24	-0.33	-0.17
P-wave velocity WGR [m/s]	6000	6360	6000	5600	6360	5500	6320	7000	6320
K value (WGR)	-	-0.025	-0.05	-0.15	-0.05	-0.15	-0.025	-0.025	-0.025
Dip angle of fault plane reflection on seismic x-line 2571	35°	39°	35°	32°	38°	28°	36°	43°	39°

Item DR3:

Details about the 2D forward modelling of gravity and magnetic data and figures illustrating several steps of the modelling process

To keep the models simple and to minimize interpretation-driven bias, the modelling process was divided into several steps, starting with a simple layer-cake geometry of the subsurface and gradually adding more structural complexity until finding the best-fit density and magnetic model. A detailed description of each modelling step is covered below.

In general, density modelling is more simple and robust than the modelling of magnetic anomalies because density variations within one rock formation are usually small whereas magnetic rock properties can vary significantly over short distances. Therefore, best-fit density models for each modelling step were developed first. The density models then formed the basis for the final magnetic model. Except for models 1 and 2, densities and susceptibilities were explicitly chosen to fit the measured anomaly curves, not to force the

model to match specific expectations and hypotheses. Input properties for models 1 and 2 represent average density and susceptibility values for WGR and Allochthon which were derived from statistical analysis of onshore petrophysical measurements.

Model 1: "Layer cake" model with constant properties for entire crystalline basement

Model 1a: Constant basement properties: D: 2.8 S: 0.01 (average for rocks of the WGR derived from petrophysical analysis)

Model 1b: Constant basement properties: D: 2.75 S: 0.003 (average for rocks of the "Allochthons" derived from petrophysical analysis)

A pronounced mismatch between modelled and observed gravity and magnetic anomaly follows from a basic layer-cake model with constant properties within the crystalline basement, implying that a uniform crustal density and magnetic susceptibility cannot explain the observed anomalies and that the basement must be structurally and compositionally more heterogeneous (Figure DR3A+B). Slight amplitude variations of the modelled gravity curve are the result of a local lateral density contrast between sediments and basement highs. The same effect is observed for the modelled magnetic anomaly curve indicated by short-wavelength amplitude peaks. The gradients of the magnetic signal are steeper than for the density curve due to a strong contrast between magnetic basement rocks and non-magnetic sediments.

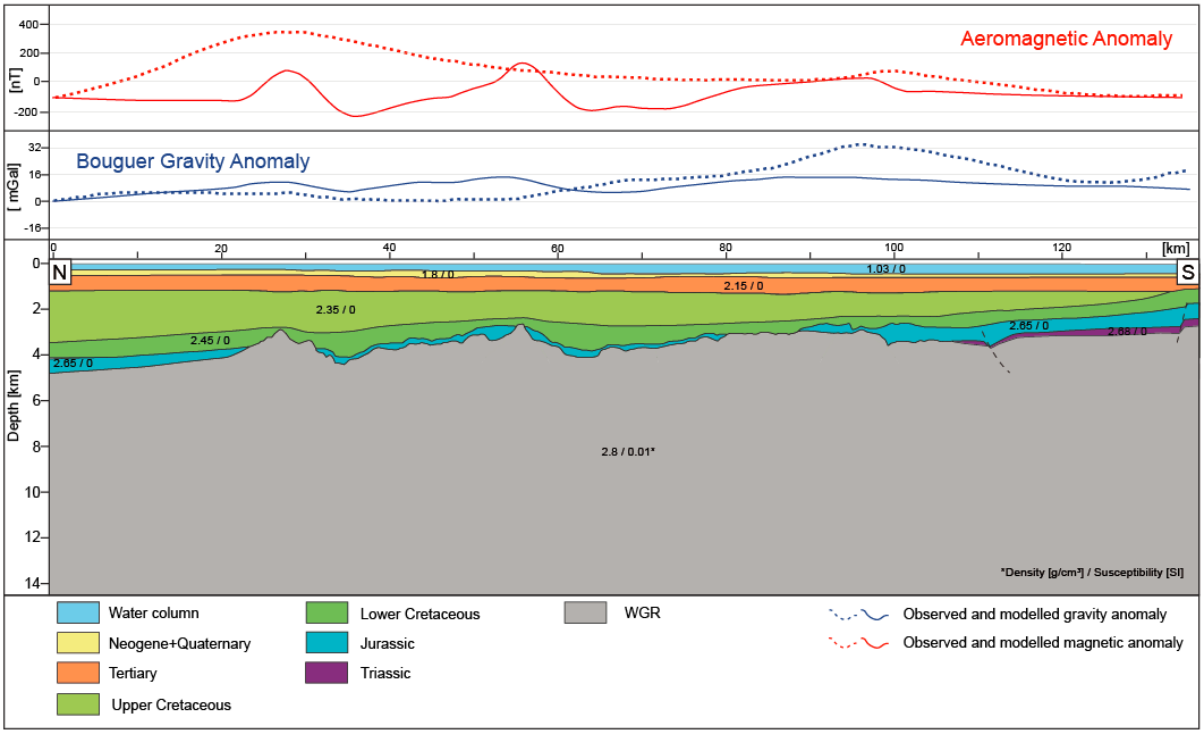

Figure DR3A: Model 1a

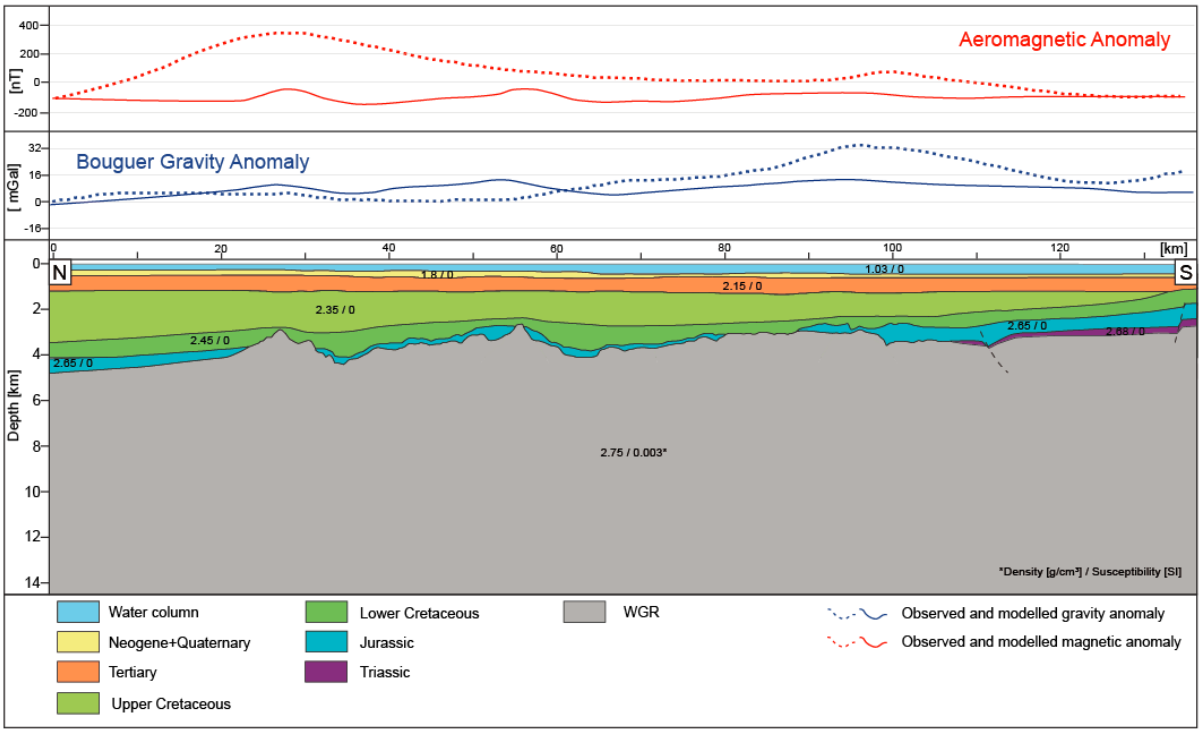

Figure DR3B: Model 1b

Model 2: Adding the interpreted Top WGR surface and dividing the basement into two rock bodies with constant properties

Constant basement properties: WGR - D: 2.8 S: 0.01/ Allochthon - D: 2.75 S: 0.003

In a second step, the basement was divided into large-scale anticlines and synclines of the WGR and overlying Allochthons using constant density and susceptibility values and geometrical relationships between both units (Figure DR3C). Despite a clear difference between model and measured anomalies, an improvement to the first model was achieved, seeing that maxima of the modelled density and magnetic anomaly curves plot in similar positions as the measured ones. However, the discrepancy between amplitudes and wavelengths of the modelled and observed anomalies indicates that density and magnetic properties have a laterally and vertically more complex distribution within basement.

In particular, the gravity curve suggests a strong contrast in density on either side of the interpreted WGR-cored anticline and decreasing densities with only minor changes along the profile to the North. On the other hand, the long-wavelength, northern magnetic anomaly suggests the presence of an additional source body at deeper levels and stronger magnetised rocks along the middle part of the profile. Consequently, a more complex subsurface model with lateral changes in density and magnetisation is required to explain the measured anomalies.

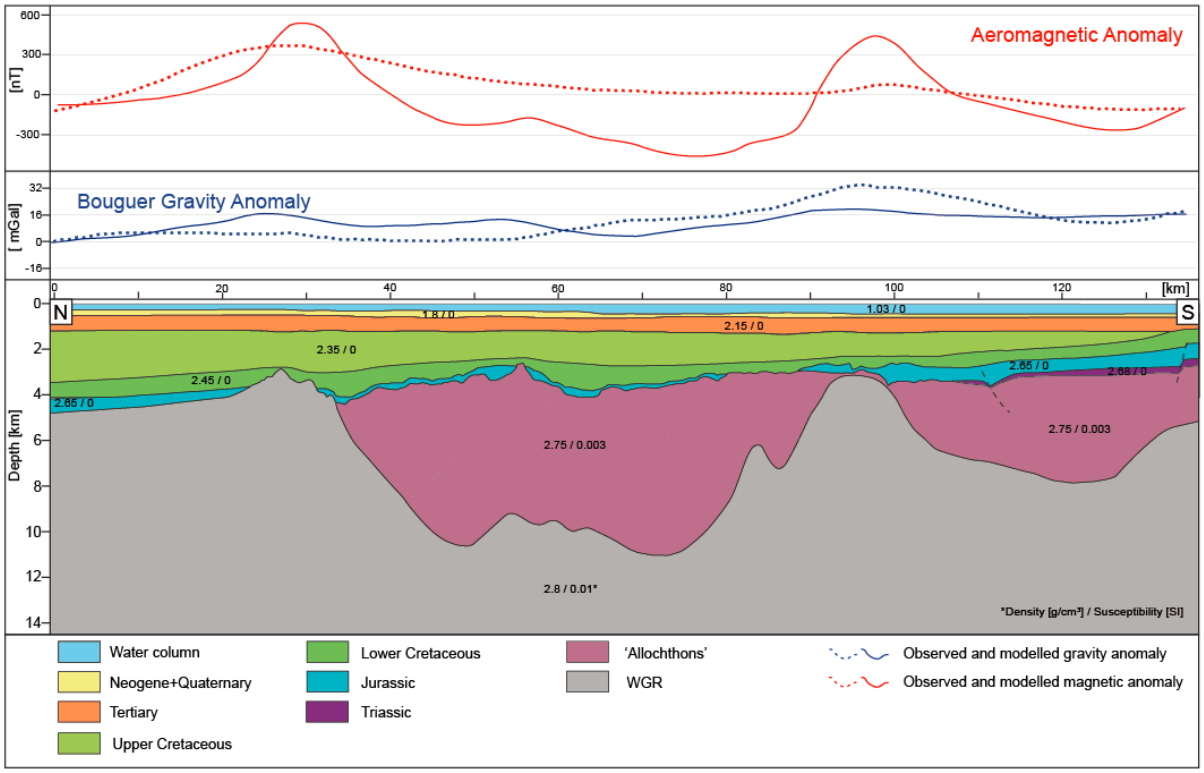

Figure DR3C: Model 2

Model 3: Best-fit density model and division of basement into separate domains based on changes in seismic reflection patterns

Based on large-scale changes in the geometry of seismic reflection patterns, the 'Allochthons' were subdivided into several blocks as indicated by the dashed lines in Figure 8 in the paper. A higher number of model blocks increases the number of possible model scenarios which are not necessarily geologically plausible. Therefore, it was decided to use the fairly well-constrained southern WGR-cored anticline as a static reference point for which a density of 2.87 g/cm^3 is required to match the distinct positive gravity anomaly, a value which is considered reasonable for high-pressure rocks within the WGR. Besides, using smaller densities for the WGR-cored anticline would require unrealistically high densities (>3.3 g/cm^3) for both blocks on either side of the anticline to still match the observed density anomaly. In the following modelling steps, a best-fit density model for the crystalline

basement was generated first (Figure DR3D) before attempting to match the magnetic anomaly curve.

The model indicates lower density values for the upper WGR in the North of the study area (2.75 g/cm^3 = average of any gneiss) which agrees with the average density distribution for the WGR onshore (Olesen et al., 2010). Note that the model does require the WGR-high in the North although it is not clearly reflected in the gravity signal amplitude. This is explained by the similar density values of adjacent basement blocks which do not cause lateral density contrasts that are large enough to cause distinct anomalies.

The density distribution within the Allochthon is more complex. An anomalously dense body (2.9 g/cm^3) is required in the central part of the profile but it has no pronounced expression in the observed anomaly curve. This dense body is defined by a zone of S-SW-dipping intra-basement reflection patterns in seismic data which have been interpreted as a shear zone/fault zone (attributed to SFRc). The increased density value might be explained by an increased abundance of mylonites, high-density mafic rocks or local HP-metamorphosed gneisses of the WGR. The model provides no unambiguous evidence for the presence of Devonian sediments in the southern part of the study area where sub-parallel, stratified reflections are observed in seismic data. The difference in density and susceptibility for Devonian sediments and allochthonous rocks appears to be too small for having a noticeable effect on the gravity anomaly.

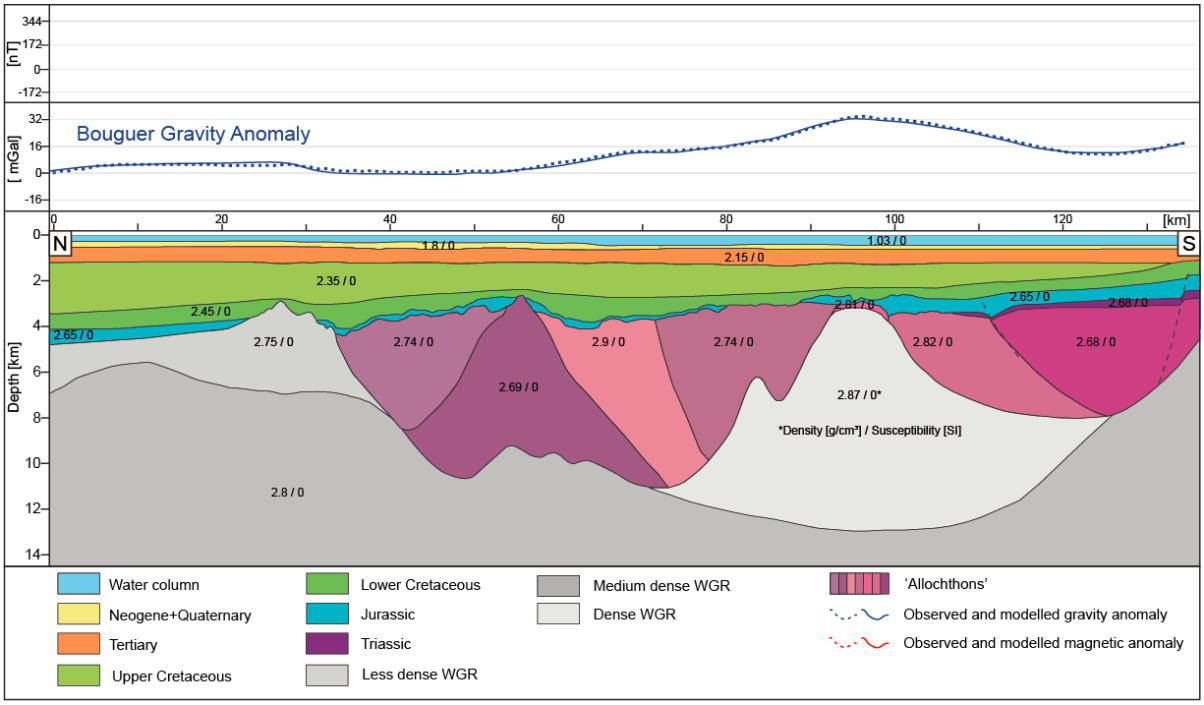

Figure DR3D: Model 3

Item DR4:

Uncertainty analysis of 2D forward modelling of gravity and magnetic data

Interpreting and forward modelling potential field data is inherently ambiguous, and the integration of additional data sets can help reduce uncertainties and better constrain models.

In the following, we list the most important factors that can introduce errors and uncertainty to 2D forward modelling of gravity and magnetic data and also suggest some actions that can be conducted to better constrain models.

<u>Factors that introduce uncertainty:</u>

- No constraints on the geometry, depth, density and magnetic susceptibility of source bodies

- If geometrical constraints are provided by e.g. a borehole-constrained seismic interpretation (in TWT), an inaccurate velocity model and depth-conversion can lead to incorrect depth estimates of the source bodies
- Unknown depth to basement and/or Moho
- Vertical variations in density and magnetic properties within source bodies may not be captured by the model
- Rock types with similar density and magnetic properties may not be distinguished
- Magnetic remanence
- Multiple, stacked, shallow and deep source bodies may create a mixed anomaly signal comprising short- and long-wavelength anomalies, respectively; these may be difficult to identify and separate
- Unfavourable selection of the model profile orientation with respect to the strike direction of the geological source body and/or gravity and magnetic anomaly leading to 3D and out-of-plane effects which are not captured in 2D models
- Data resolution; low resolution potential field anomaly data may not represent shallow, short-wavelength anomalies very well

<u>Actions we conducted to reduce uncertainties:</u>

- Constrain the geometry of the model by using e.g. well-constrained, depth-converted seismic interpretation
- If available, use density and magnetic properties of sediments and crystalline rocks present in the area
- Consider the combination of different density and susceptibility values to limit the possible choices of rock types

- Choose model profile location perpendicular to the trend of the geological feature and/or contours of the gravity and magnetic anomaly
- Extend the model profile beyond the seismic profile to eliminate any edge effects and to better control deep, long-wavelength anomalies and absolute Moho depth
- Include transformations and derivatives of the anomaly signals in the modelling process to help distinguishing between deep and shallow sources
- Create additional model profiles which are parallel to each other (semi-3D) and/or include models which form tie-lines between 2 or more parallel profiles

Item DR5:

Large-scale version of seismic profile shown in Figure 7.

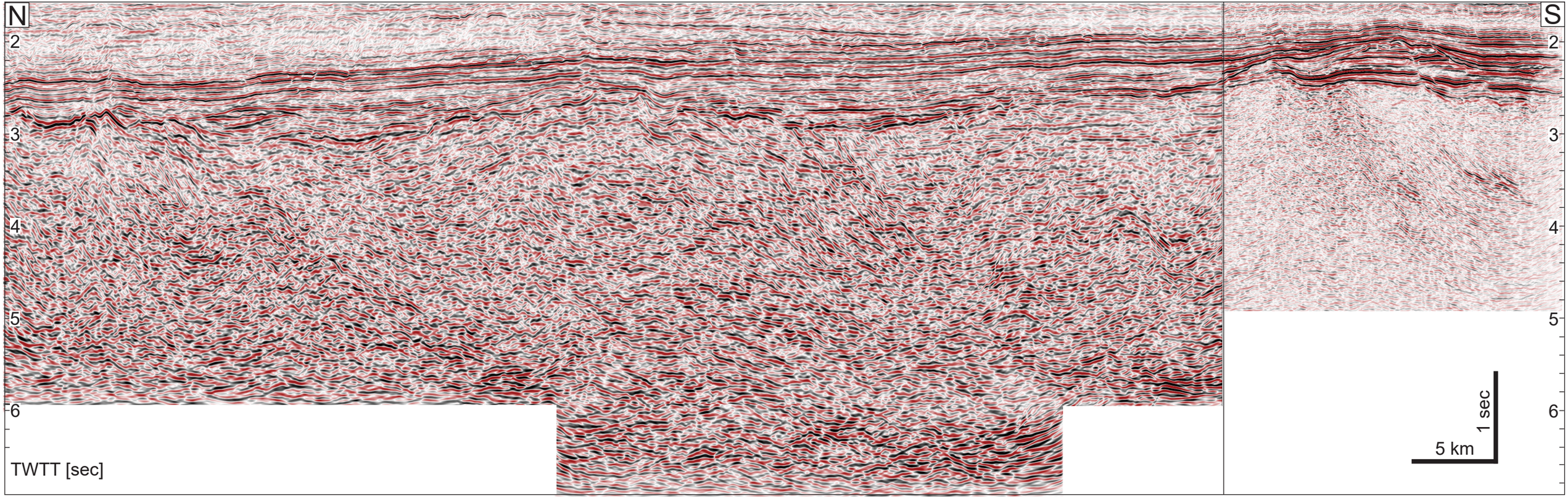
N
S
2
3
4
5
6
TWTT [sec]
1 sec
5 km

Item DR6:

Crystalline basement cores recovered from boreholes 6306/10 and 6305/12-2 and their location in relation to strong positive magnetic anomalies along the western Norwegian margin.

Both cores are characterised by a granitic composition and texture. Greenish colour of quartz and feldspar crystals in core 6305/12-2 probably due to hydrothermal alteration.